Check for updates

CLIMATOLOGY

Quantifying the impacts of rainfall and evaporation on Lake Bonneville

John Mering[1]†, Alexandrea J. Arnold[2]†*, Lauren Chari[1], Hung-I Lee[2], Jory Lerback[1], Osinachi Ajoku[3], Daniel E. Ibarra[4], Stephen Nelson[5], Alexander Farnsworth[6], Paul Valdes[6], Aradhna Tripati[1,2,6,7,8,9]*

Copyright © 2026 The Authors, some rights reserved; exclusive licensee American Association for the Advancement of Science. No claim to original U.S. Government Works. Distributed under a Creative Commons Attribution NonCommercial License 4.0 (CC BY-NC).

Improved understanding of hydroclimatic drivers in water-stressed regions enables more accurate forecasting of future climate change impacts. Lake Bonneville was the largest Pleistocene lake in western North America, with a maximum surface area of ~52,000 km^2, before shrinking markedly to become the modern Great Salt Lake. After more than a century of study, the balance between enhanced precipitation and reduced evaporation as drivers of lake growth continues to be debated. Multiple studies identify precipitation as the main factor associated with the highest lake levels, but most proxies provide an estimate of net evaporation and cannot independently resolve precipitation from evaporation. Therefore, factors associated with lake size, growth, and retreat remain uncertain. This study uses the thermodynamically based carbonate clumped isotope geothermometer to estimate temperature, evaporation, and precipitation at Lake Bonneville from 23 to 16 thousand years ago (ka). Clumped isotope derived constraints on hydroclimate are also applied to assess the accuracy of regional climate model outputs. During transgressive and open phases of the lake, we find that regional and large-scale precipitation delivery were the driving factors of lake expansion. In contrast, at its maximum extent (~17.5 ka), Lake Bonneville was maintained via suppressed evaporation rates at 50% relative to modern while precipitation rates were similar to modern levels.

INTRODUCTION

During the Late Pleistocene, lakes expanded throughout the Great Basin, from southern Oregon to Mexico, with pluvial maxima occurring between 25 and 15 thousand years ago (ka) [e.g., Gilbert (*1*), Hostetler *et al.* (*2*), Reheis *et al.* (*3*), and McGee *et al.* (*4*)]. Lake Bonneville was the largest pluvial lake within the Great Basin during the Late Pleistocene, reaching a maximum extent of 52,110 km^2 shortly after the Last Glacial Maximum (LGM; 23 to 18 ka) (*5*). Because of the sheer size of the ancient lake as indicated by lacustrine geomorphic features, Bonneville has been of longstanding interest, with the first publication reporting it by Gilbert (*1*).

Despite over a century of study, the hydrologic factors that sustained the size of the lake and were associated with the lake's growth and subsequent regression to the modern Great Salt Lake remain ambiguous. Insights gained from understanding the past evolution of Lake Bonneville can help constrain the modern water balance of the Great Salt Lake and support more accurate predictions of the impact of climate change and other anthropogenic drivers on lake evolution. Constraints on past hydroclimatic drivers can also reduce uncertainty in simulations from climate models. Data model comparisons on paleo-lakes can improve our understanding of regional and synoptic-scale atmospheric circulation patterns and underlying mechanisms of change. In addition, understanding of past changes in regional hydroclimate helps to interpret paleoenvironments of Indigenous peoples. In this region, the Goshute, whose ancestors have lived here since time immemorial, have some of the earliest archeological evidence for land relations dating back to ~13 ka (*6*).

Lake Bonneville began its transgression from a saline, ephemeral body to a large, freshwater lake around ~24 ka (*7*). The hydrographically closed basin filled to 1370 meters above sea level (m.a.s.l.) by ~23 ka, when it formed the Stansbury shoreline (*7*). By about ~18 to 17.5 ka, it reached a maximum elevation of 1552 m.a.s.l with depths exceeding 300 m in some locations, forming the Bonneville shoreline (*8*). Following this pluvial maximum, the lake began to overflow across the surface of an alluvial fan that eroded the sediments underneath, creating instability in the underlying deposits, initiating the formation of a larger outlet and the rapid loss of a large volume of water, known as the Bonneville flood, which occurred between ~18 and 17.5 ka (*8*). The outflow triggered a 100-m drop in lake levels and a transition to a hydrologically open basin, where the Provo shoreline subsequently formed during a sustained overflowing phase, likely between ~18 and 15 ka, although the precise timing and duration remain debated (*9*). Lake Bonneville continued to shrink (*1*), with a short lived 15-m rise at 12.7 ka termed the Currey cycle (*10*). The current lake remnants, termed the Great Salt Lake, refer to when it reached an elevation of ~1280 m.a.s.l at ~13 ka (*10*, *11*).

Climate model analysis has been used to argue that synoptic-scale moisture transport was the primary factor causing the large size of Lake Bonneville and associated lake effect precipitation (*2*). Antevs (*12*) hypothesized that the North American Ice Sheet promoted the southward deflection of the mean position of the mid-latitude jet stream, diverting storm tracks and enhancing winter rainfall across western North America (*12*). An alternative hypothesis holds that the timing of lake elevation maxima reflects enhanced

[1]Department of Earth, Planetary and Space Sciences, University of California, Los Angeles, Los Angeles, CA 90095, USA. [2]Department of Atmospheric and Oceanic Sciences, University of California, Los Angeles, Los Angeles, CA 90095, USA. [3]Department of Atmospheric Sciences, Howard University, Washington, DC 20059, USA. [4]Department of Earth, Environmental and Planetary Sciences, Brown University, Providence, RI 02912, USA. [5]Department of Geology and Geophysics, University of Utah, Salt Lake City, UT 84112, USA. [6]School of Geographical Sciences, University of Bristol, Bristol, UK. [7]Institute of the Environment and Sustainability, University of California, Los Angeles, Los Angeles, CA 90095, USA. [8]American Indian Studies Center, Chicano Studies Research Center, University of California, Los Angeles, Los Angeles, CA 90095, USA. [9]School of Earth Sciences, University of Bristol, Bristol, UK.
*Corresponding author. Email: ajarnold1@g.ucla.edu (A.J.A.); atripati@g.ucla.edu (A.T.)
†These authors contributed equally to this work.

Downloaded from https://www.science.org at Brown University on January 25, 2026

rainfall associated with both the mean southward displacement of the jet and transient reorganizations of the jet during stadial intervals (e.g., Heinrich Event 1) (*13*). The existence of a possible teleconnection with the North Atlantic that affected precipitation in the region could explain why montane glaciers in the Wasatch and Uinta Mountains, east of the Bonneville basin, also retreated and advanced contemporaneously with the North American Ice Sheet (*14*–*16*). However, recent analyses of deglacial climate simulations suggests that western North American precipitation and the mid-latitude jet are not always collocated and that their relationship changed through the deglaciation (*17*).

Not all studies identify winter storms as the most likely cause for pluvial maxima in the region. Lyle *et al.* (*18*) reported that many lakes in the northern Great Basin did not achieve their highest elevations until after the LGM, while lakes in the southern Great Basin expanded before and during the LGM and identified the Sierra Nevada and Cascade Mountains as strong barriers that would have inhibited transport of moisture inland from the coast into the central and northern Great Basin. They argued that a strengthened summer monsoon from the tropical East Pacific could have penetrated further north, providing additional moisture to advance lakes; however, they do not provide a mechanism for increased northward monsoon activity (*18*). In addition, although much work has focused on precipitation in the water budgets in the Great Basin, diminished evaporative loss during cooler stadial summers has also been identified as a driver for the advance of many lake systems across the region (*19*–*21*). A potential role of lake effect precipitation has also been proposed (*2*).

Unambiguous proxy data are critical for resolving the factors influencing the hydrologic budget of the lake and quantifying their contributions to water budgets. Yet, most terrestrial proxies that reflect net precipitation (e.g., lake level), are subject to multiple assumptions (e.g., $\delta^{18}O$ and δD-based reconstructions) and/or are sensitive to changes in species composition (e.g., pollen). Hence, the climatic conditions required to sustain large lakes in the Great Basin remain underdefined.

Here, we use a thermodynamically based proxy to evaluate the paleohydrologic framework for Lake Bonneville. Carbonate clumped isotopes have been shown to provide a direct constraint on the temperature of lacustrine carbonate mineral formation, which conventional oxygen isotope techniques cannot accurately quantify in terrestrial settings alone due to the potential for changes in meteoric and lake water $\delta^{18}O$ (*22*–*24*). We apply the carbonate clumped isotope proxy to lacustrine archives and reconstruct lake surface temperatures and water $\delta^{18}O$ and use these clumped isotope–derived estimates to calculate mean annual air temperature (MAAT), evaporation, and precipitation rates and determine controls on lake water balance. We also compare results to climate models and discuss the implications of our work for the global- and local-scale atmospheric mechanisms for this water balance.

RESULTS

Stable and clumped isotope analysis of shoreline sediments

A total of 49 samples from ~23 to ~16.5 ka were analyzed for carbonate clumped isotopes. Samples of 36 individual gastropod shells from six sites, representing two species (*Pyrgulopsis bonnevillensis* and *Stagnicola bonnevillensis*), two marl samples, and 11 tufa samples spanning the Stansbury, Bonneville, and Provo shorelines (Fig. 1) were analyzed for $\delta^{13}C$, $\delta^{18}O$, and clumped isotope composition, Δ_{47} (Table 1 and see Materials and Methods). For gastropod and marl samples, we report basin averages, whereas tufa data are presented as shoreline-specific averages. Table S1 contains all geochemical data for the sample set. Δ_{47}-derived water temperatures were used in concert with a transfer function to construct MAAT (*25*) estimates and used within a hydrologic modeling framework to calculate precipitation and evaporation rates (see Materials and Methods). Oxygen isotopic composition of lake water ($\delta^{18}O_{water}$) was calculated using temperatures derived from Δ_{47} analysis, measured carbonate $\delta^{18}O$, and a mineralogy-dependent equilibrium temperature. All $\delta^{18}O_{water}$ values are reported relative to the Vienna Standard Mean Ocean Water (V-SMOW) standard, and water isotope reconstructions in this work are reported with a correction applied to account for enrichment of ^{18}O in the glacial ocean during the LGM (*26*). We use results of hydroclimatic change at Lake Bonneville to partition the thermodynamic and dynamic contributions to lake level changes (see Materials and Methods) and compare to climate model output.

DISCUSSION

MAAT at Lake Bonneville

Figure 2A shows the evolution of Δ_{47}-T at Lake Bonneville. Cooling was associated with the growth of Lake Bonneville ~23.4 to 22.8 ka (i.e., the formation of the Stansbury shoreline during transgressive phase of the Stansbury Oscillation). Tufa-derived estimates of the MAAT anomaly relative to modern associated with the Stansbury shoreline are 6.9° ± 1.3°C. Basin-average gastropod and marl Δ_{47}-T increase by roughly ~1°C in the subsequent transgression, with average MAAT anomalies of 5.2° ± 0.5°C, 6.0° ± 1.2°C, and 5.6° ± 0.5°C for Bonneville basin gastropods, Sevier sub-basin gastropods, and Bonneville basin marls, respectively. Cooling continues to ~17.5 ka (the formation of the Bonneville shoreline during the Lateglacial), with a maximum temperature depression of 9.3° ± 1.5°C lower than modern, followed by ~3.4°C warming by ~16.5 ka (formation of the Provo shoreline). MAATs were consistently depressed across much of the Bonneville lake cycle, both before, during the closed basin, and post-LGM open basin phases of the lake (Fig. 2A and Table 2). Δ_{47}-T (this study) indicate a similar degree of cooling to vegetation-based proxies (6° to 7°C) (*27*) and packrat midden macrofossil reconstructions (6.2°C) (*28*), while amino acid racemization supports more cooling (10°C) (*21*).

Regional rainfall and evaporation changes

These Δ_{47}-results allow us to confidently quantify not only changes in temperature but also precipitation and evaporation rates and separate out controls on effective precipitation (Table 2). Modern precipitation rates are ~344 mm/year (30-year normals for 1991 to 2020) (*29*). The first major precipitation forcing at Lake Bonneville occurs between 23 and 22 ka, following Heinrich Stadial 2 (HS2; ~24 ka) (Fig. 2), with evidence for an increase in precipitation by a factor of 2.2 to 2.9 times modern, concurrent with a ~90 m rise in lake level (*7*). The second large precipitation forcing observed in our reconstructions is between ~17.5 and ~16.5 ka, with values increasing from ~1.5 to 1.8× modern values, concurrent with HS1 (~18 to 14.7 ka) and pluvial maxima in other parts of the northern Great Basin (*4*, *13*, *20*).

Modern lake evaporation rates of 1299 mm/year are calculated by combining a pan coefficient of 0.9 from Matsubara and Howard (*30*) and average pan evaporation rates for all sites in the Bonneville basin

Downloaded from https://www.science.org at Brown University on January 25, 2026

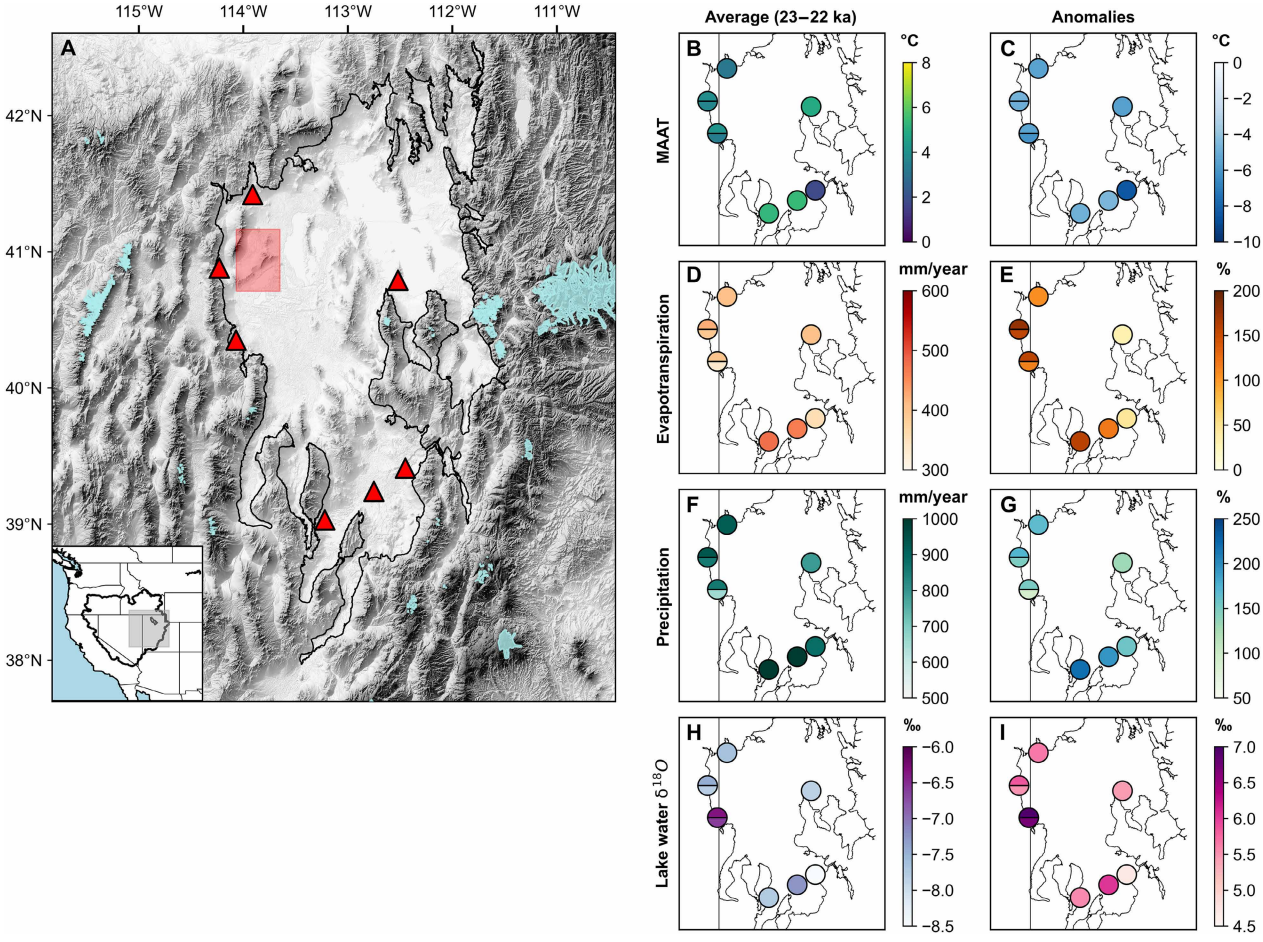

Fig. 1. Maps showing reconstructed hydroclimate parameters derived from clumped isotopes for the LGM. Both LGM values (23 to 22 ka) and LGM-modern anomalies are shown. (**A**) Location of Lake Bonneville and nearby glaciers during the Pleistocene. Red triangles represent sampling locations for gastropods and marls. Red shaded square represents where a suite of tufas were collected for the Stansbury (~23 ka), Bonneville (~17.5 ka), and Provo (~16.5 ka) shorelines. Light blue areas indicate extent of LGM glaciers. Black shaded square in inset represents study area in map; black outline in inset represents the extent of the Great Basin region. (**B** and **C**) MAAT, (**D** and **E**) precipitation, (**F** and **G**) evapotranspiration, and (**H** and **I**) lake water $\delta^{18}O$. Half circles show results from colocated gastropods (top) and marl (bottom). MAAT anomalies are calculated using site-specific modern MAAT [30-year normals (1991 to 2020)] (*29*). Modern evapotranspiration rates used to calculate anomalies use site-specific average annual evapotranspiration from 1958 to 2015 (*80*). Precipitation anomaly is calculated using average modern precipitation rates over the entire Bonneville basin [344 mm/year; 30-year normals (1991 to 2020)] (*29*). Lake water $\delta^{18}O$ anomaly is calculated relative to modern volume-weighted precipitation $\delta^{18}O$ over the Bonneville basin (−13.3‰) based on monthly $\delta^{18}O$ values (*77*) and 30-year averages for monthly precipitation (*29*) across all sample sites. All LGM results are derived from gastropods and marls.

Table 1. Isotopic data for Lake Bonneville. Site averages shown for each carbonate type. Uncertainties reported are 1 standard error. Individual sample data is reported in table S1.

Basin/Shoreline	Sample type	Age	$\delta^{13}C$ (V-PDB, ‰)	$\delta^{18}O$ (V-PDB, ‰)	Δ_{47} [InterCarb-Carbon Dioxide Equilibrium Scale (I-CDES), ‰]	T_{water} (°C)	$\delta^{18}O_{water}$ (V-SMOW, ‰)
Bonneville basin	Gastropod	22.6 ± 0.6 (transgressive)	1.6 ± 0.2	−5.1 ± 0.1	0.639 ± 0.004	9.5 ± 0.5	−7.3 ± 0.3
Sevier sub-basin	Gastropod	22.4 ± 0.2 (transgressive)	−1.0 ± 0.5	−4.6 ± 0.2	0.643 ± 0.002	8.5 ± 1.2	−7.9 ± 0.4
Bonneville basin	Marl	22.2 ± 0.1 (transgressive)	−1.2 ± 0.2	−4.5 ± 0.1	0.641 ± 0.003	15.2 ± 0.5	−7.2 ± 0.6
Stansbury shoreline	Tufa	23.1 ± 0.3 (transgressive)	−1.1 ± 0.5	−4.3 ± 0.2	0.641 ± 0.008	11.5 ± 1.3	−4.9 ± 0.3
Bonneville shoreline	Tufa	17.5 ± 0.5 (transgressive)	−0.7 ± 0.0	−4.4 ± 0.0	0.633 ± 0.008	9.5 ± 1.3	−5.4 ± 0.5
Provo shoreline	Tufa	16.5 ± 1.5 (open)	0.1 ± 0.2	−4.6 ± 0.1	0.638 ± 0.004	12.6 ± 0.9	−5.3 ± 0.3

Downloaded from https://www.science.org at Brown University on January 25, 2026

(~1434 mm/year; table S4) (*31*). Carbonate clumped isotope water balance results suggest that evaporation rates were consistently reduced throughout the LGM and deglacial (to 0.5 to 0.8× modern values) and were the dominant factor (compared to precipitation) driving Lake Bonneville's growth and regional lake and glacial maxima. Early LGM precipitation rates (Stansbury tufa; ~23 ka) were similar to modern (8% increase relative to modern), while lake evaporation rates were substantially (~35%) lower than modern (Fig. 2, B and C). This suggests that, at least initially, decreased temperatures that suppressed evaporation, instead of large increases in precipitation, were the dominant factor that led to Lake Bonneville's growth.

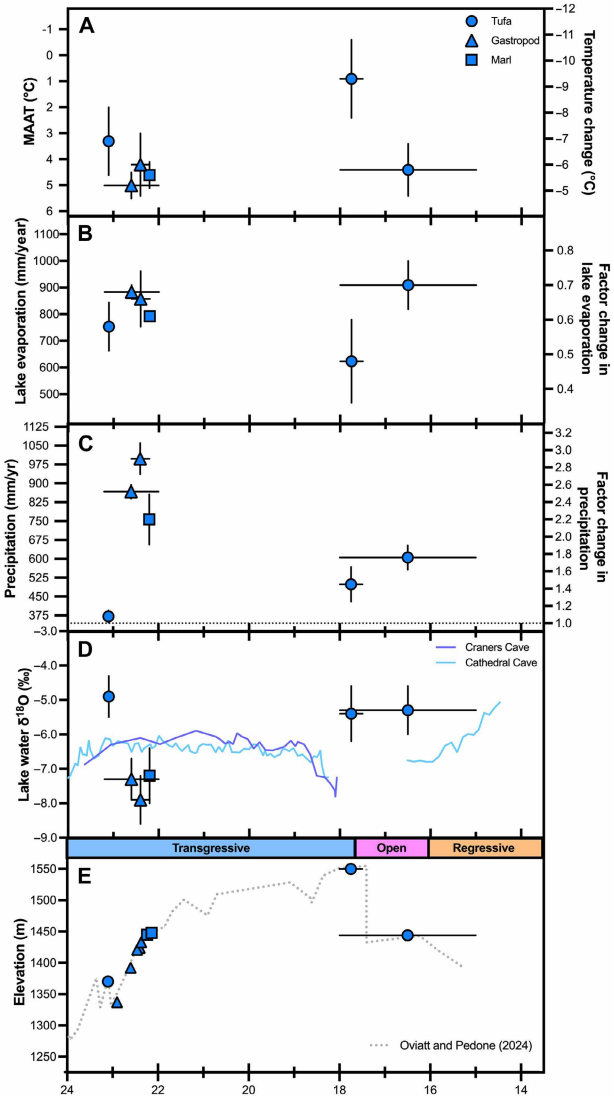

Fig. 2. Evolution of hydroclimates at Lake Bonneville from 23 to 16 ka. Error bars = 1 standard error. Age estimates for tufas represent the youngest potential age of the shoreline (*7*). (**A**) Δ_{47}-T anomaly for samples and reconstructed MAAT. See Materials and Methods for description of calculations and errors. (**B**) Δ_{47}-derived factor changes in lake evaporation and lake evaporation rates. (**C**) Δ_{47}-derived factor changes in precipitation and precipitation rates. (**D**) Δ_{47}-derived water $\delta^{18}O$, corrected for ice volume. Purple and light blue lines show lake water $\delta^{18}O$ values calculated from lacustrine cave carbonate data (*32*). A water temperature of 4°C is applied to cave carbonates, which formed in the deep lake, reflecting the temperature at which fresh water attains maximum density. (**E**) Hydrograph for Lake Bonneville based on isostatically corrected elevations (*7*).

During the subsequent LGM transgression from ~23 to 22 ka of ~90 m (*7*), while evaporation rates remained consistently suppressed, at 24 to 27% lower than modern (Fig. 2E), gastropod-derived values support almost a tripling of precipitation values, with increases of 153 to 190% relative to modern values. Thus, while increased evaporative suppression was a factor contributing to lake growth, coupled increases in precipitation contributed to large lake area increases during the LGM. Estimates from slightly younger marl samples from the same site suggest lower evaporation rates (32% lower than modern) and less precipitation (120% increase relative to modern) compared to the results from gastropods; we note that gastropods may reflect shorter-term changes in precipitation in comparison to tufa and marls, which integrate over the longer time intervals during which they form. Thus, in contrast to ~23 ka (the Stansbury interval), increases in precipitation become a more dominant factor driving lake growth in the early LGM.

Tufas from ~17.5 ka (Bonneville shoreline) formed during the highest levels of the lake support smaller increases in precipitation, with reconstructions supporting increases of 45% relative to modern. However, during this time, tufa data support almost a halving of modern evaporation rates (47% decrease). Thus, short-lived increases in precipitation between 23 and 22 ka, coupled with a temperature-driven reduction in evaporation, drove the notable growth of Lake Bonneville to its maximum extent during its transgression.

During the regressive phase of the lake around ~16.5 ka (Provo shoreline), there is evidence for increased precipitation (61% greater than modern). We note that during this interval, the lake was hydrologically open with an outflow during this time, but the lake sustained a relatively consistent elevation. Thus, our estimates derived here should be treated as a minimum. However, results indicate that increasing lake evaporation rates (78% of modern values) were critical for setting the water balance. In summary, we suggest that reduced evaporation was critical for the large size of the lake, but that a short-lived wetter state persisted during the early LGM and following the maximum extent at ~17.5 ka (Bonneville shoreline).

Temporal evolution of $\delta^{18}O_{water}$

Figure 2D shows the temporal evolution of lake water oxygen isotopic composition of Lake Bonneville that should reflect changes in moisture source and delivery. Average $\delta^{18}O_{water}$ values for ~23 ka (Stansbury shoreline) tufa (~23 ka) is -4.9 ± 0.3‰. Average $\delta^{18}O_{water}$ estimates decrease following the Stansbury Oscillation (~23 to 22 ka) for Bonneville basin gastropods and marls (-7.3 ± 0.6‰ and -7.2 ± 0.6‰, respectively) and the Sevier sub-basin gastropods (-7.9 ± 0.4‰). $\delta^{18}O_{water}$ increases toward ~17.5 ka (Bonneville shoreline), with estimates from a suite of tufas resulting in a composition of -5.4 ± 0.5‰ and remains similar through ~16.5 ka (Provo shoreline; -5.3 ± 0.3‰).

Changes of up to 2.9‰ in $\delta^{18}O_{water}$ occurred between 23 and 22 ka (i.e., between the development of the Stansbury shoreline and gastropod and marl samples from the transgression following the Stansbury Oscillation). Between these intervals in the early LGM, we reconstruct a coeval reduction in $\delta^{18}O_{water}$ without substantial changes in Δ_{47}-MAAT, suggestive of dynamical changes being the primary driver of precipitation delivery into the basin (Fig. 2D). Comparison of these Δ_{47}-derived data from shoreline environments at Lake Bonneville to deep-water carbonate deposits from Craners and Cathedral Caves in the Bonneville basin (*32*) shows that

Downloaded from https://www.science.org at Brown University on January 25, 2026

shoreline tufas yield comparatively enriched $\delta^{18}O_{water}$, and shoreline gastropod and marl samples lower $\delta^{18}O_{water}$ values, relative to cave carbonates (Fig. 2D). Although deepwater carbonates have potential to be influenced by groundwater discharge, the incorporation of relatively depleted groundwater into cave deposits would cause decreases in $\delta^{18}O_{water}$. Thus, regardless, the shift we see in the data suggests different conditions prevailing between the surface and lake at depth. The decreases in reconstructed $\delta^{18}O_{water}$ recorded in gastropod and marl samples could be interpreted to reflect increases in precipitation or runoff rates or changes in dominant moisture source, with moisture from the North Pacific Storm track being more depleted (*33*), or moisture seasonality, with more depleted precipitation occurring during boreal winter. This hypothesis is supported by 2.2 to 2.9 times modern reconstructed precipitation rates coeval with the decrease in $\delta^{18}O_{water}$.

Our estimates of $\delta^{18}O_{water}$ for the ~17.5 ka (Bonneville shoreline) and ~16.5 ka (Provo shoreline) tufas remain stable despite an increase in reconstructed MAAT of 4°C and a 24% increase in reconstructed evaporation rates, relative to modern. In contrast, the deep-water cave deposits (*32*) could indicate an increase in $\delta^{18}O_{water}$ during the open to closed basin transition from ~17.5 to 16 ka, between the Bonneville to the Provo phase. It is possible that increasing $\delta^{18}O_{water}$ values inferred from ~16.5-ka deep-water cave carbonates may be due to enhanced mixing from depth associated with the lake regression after the Bonneville flood; this may have been counterbalanced in shoreline settings by increased evaporative enrichment associated with warmer conditions, resulting in minimal change in $\delta^{18}O_{water}$.

Comparison to nearby glaciological and hydrological modeling

Quirk *et al.* (*15*) calculated the combinations of temperature depression and precipitation change needed to sustain a series of glaciers in the Wasatch Mountains, east of Lake Bonneville (Fig. 3A). Their work suggests a 9° to 11.5°C temperature suppression between 21

Table 2. Hydroclimate parameters derived from clumped isotopes. Basin averages shown with 1 standard error. Modern MAATs are 30-year normals from 1991 to 2020 (*29*). Precipitation anomalies were calculated using 30-year normals from 1991 to 2020 over the basin area, yielding a modern precipitation of 344 mm/year (*29*), which is comparable to values derived for the basin using reanalysis data (338 mm/year) (*34*). Modern lake evaporation rates used to calculate evaporation anomalies were calculated using a pan coefficient of 0.9 (*29*) and the average modern pan evaporation rate from 13 sites located within our study area (table S4).

Basin/shoreline	Sample type	Modern MAAT (°C)	Estimated MAAT (°C)	MAAT Anomaly (°C)	Lake evaporation (mm/year)	Anomaly (%)	Precipitation (mm/year)	Anomaly (%)
Bonneville basin	Gastropod	9.3	4.5 ± 0.5	−5.2 ± 0.5	988 ± 35	−24 ± 3	868 ± 27	153 ± 6
Sevier sub-basin	Gastropod	10.1	4.2 ± 1.2	−6.0 ± 1.2	951 ± 21	−27 ± 9	997 ± 62	190 ± 18
Bonneville sub-basin	Marl	9.1	3.5 ± 0.1	−5.6 ± 0.5	883 ± 19	−32 ± 1	757 ± 101	120 ± 29
Stansbury shoreline	Tufa	10.2	3.3 ± 1.3	−6.9 ± 1.3	840 ± 106	−35 ± 8	372 ± 24	8 ± 7
Bonneville shoreline	Tufa	10.2	0.7 ± 1.8	−9.3 ± 1.5	693 ± 172	−47 ± 13	499 ± 67	45 ± 20
Provo shoreline	Tufa	10.2	2.2 ± 1.2	−5.8 ± 10	1009 ± 98	−22 ± 8	605 ± 47	76 ± 14

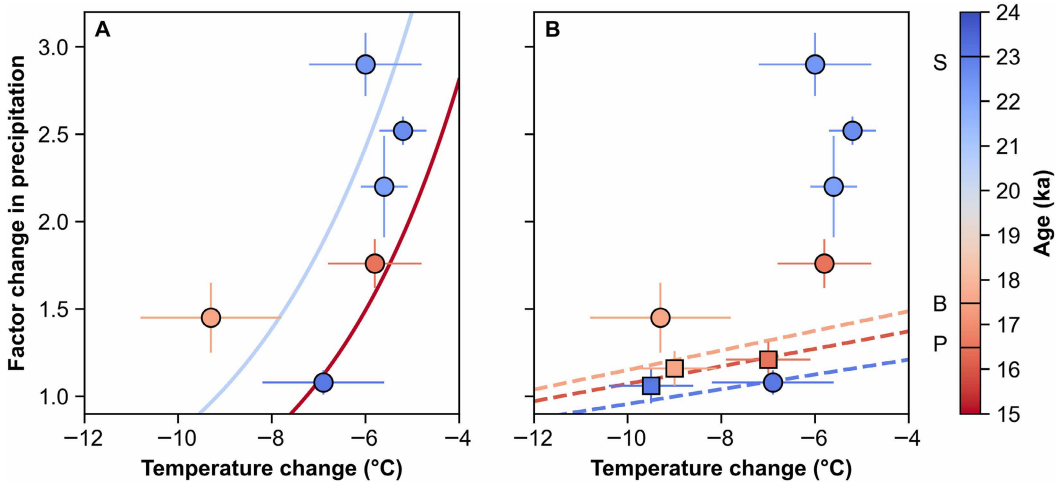

Fig. 3. Comparison of clumped isotope estimates of temperature and precipitation changes since the LGM from shoreline tufa to other approaches. (**A**) Comparison of Δ_{47}-derived values (circles) to glaciological calculations (solid lines) and (**B**) comparison to hydrologic modeling (dashed lines). The *x* axis represents the temperature change estimated from the LGM to modern (Table 2) (*29*). The *y* axis represents the ratio of reconstructed precipitation relative to modern precipitation over the Bonneville basin (P_{modern} = 344 mm/year) (*29*). Samples are color coded by age, and the S, B, and P labels on the color bar represent the midpoint ages of the estimated temporal ranges associated with Stansbury, Bonneville, and Provo phases of the lake, respectively. Solid lines in (A) are derived from glacial modeling in the Wasatch Range in (*15*). Squares in (B) are estimates from derived from the intersection of values derives from glacial modeling in (A) and a hydrologic balance model in (*35*). Dashed lines in (B) are temperature and precipitation change combinations necessary to sustain Lake Bonneville the Stansbury, Bonneville, and Provo shorelines in (*34*).

Downloaded from https://www.science.org at Brown University on January 25, 2026

and 20 ka with little to no precipitation change relative to modern during the LGM. The degree of temperature change constrained by the Bonneville tufas compare favorably to the reconstructed glacial temperature change during the LGM; however, our results suggest a 45% increase in precipitation relative to modern. Gastropods and marls from the rapidly transgressing phase of Lake Bonneville (23 to 22 ka) estimate a much higher degree of precipitation but mirror the shape of the potential precipitation and temperature combinations derived from LGM glacial moraines. Glacial modeling of the late deglacial (18 to 15 ka) suggests warming, with a doubling of precipitation relative to modern values, exhibiting excellent agreement between results from tufa from the Provo shoreline (~16.5 ka).

Figure 3B compares our estimates of precipitation and temperature changes from this study with hydrologic modeling estimates from (*34*). The Bonneville and Provo highstands are in agreement with modeling estimates derived from the temperature and precipitation combinations needed to sustain lake area and volume at each of the three prominent shorelines. The estimates derived in this study suggest higher amounts of precipitation change relative to modern except for the estimates derived from the Stansbury; however, due to the open nature of Lake Bonneville during these times, values from hydrologic balance modeling are suggested to be minimums. In addition, precipitation estimates from Belanger *et al.* (*35*), which rely on the intersection of glaciological reconstructions in Quirk *et al.* (*15*) and hydrologic modeling, suggest smaller increases in precipitation than in this study. However, their estimate of temperature change for the Bonneville highstand agrees with our reconstruction, supporting the notion that temperature-driven reduction in evaporation was a critical factor in the growth of Lake Bonneville to its maximum extent (Fig. 3B).

Climate model evaluation

We compare our Δ_{47} results to long-term mean climatological data output from 17 models. These models are from the Paleoclimate Modeling Intercomparison Project Phase 3 and 4 (PMIP3 and PMIP4) models and from a model from the Hadley Center (HadAM) run at four different resolutions to assess process representation in climate models during the LGM. To quantitatively gauge model performance using paleoclimate proxies from the LGM interval, we use skill score (SS) as a metric to assess whether or not these simulations accurately reflect hydroclimates. Results should be interpreted as a model's skill in depicting past climatic changes with respect to the null hypothesis, of no change between the LGM and modern. A perfect simulation would have a score of 1, a score of 0 would indicate that the model and reference state (no change) perform equally well, and a negative score would indicate that model error is greater than in the case of the null hypothesis. An SS that is undefined occurs when the model agrees with the data more closely than the errors in the data indicate is possible, which may be a sign of overestimation in proxy error (*36*, *37*). We use site-specific averages and basin averages to assess model skill in the 17 models.

For site-specific averages, almost all models have a positive SS with respect to temperature change since the LGM, indicating reasonable agreement. Values range from −0.25 to 0.76 (Fig. 4, fig. S2, and table S3). With the HadAM model, skill at simulating temperatures improves with resolution (Fig. 4).

For changes in evapotranspiration, most models perform poorly. Only six models exhibit positive skill, with a maximum score of 0.34. Resolution alone does not substantially improve SS with the HadAM model. While the reconstructions for all sites suggest increases in evapotranspiration relative to modern, likely due to increased moisture availability due to an extensive lake present, the majority of models simulate reduced evapotranspiration during the LGM due to lower temperatures (fig. S8). Most models do not represent the modern Great Salt Lake in preindustrial simulations, and all models do not have a representation of Lake Bonneville.

Overall, all models underestimate the precipitation forcing that is observed within the proxy dataset. Proxy-derived precipitation changes range from ~450 to 750 mm/year; however, most models simulate much smaller changes in precipitation (fig. S5). SSs range from −0.28 to 0.41, with four models exhibiting negative skill (Fig. 4). The HadAM model exhibits decreasing skill as model resolution increases, with estimates of precipitation change reduced at higher resolution. Thus, models simulate the largest increases in precipitation to perform the best.

Table 3 shows that SSs was assessed using basin averages. In this case, basin skill is calculated using an average for gastropods in the Bonneville basin, marls in the Bonneville basin, and gastropods in the Sevier basin. Similar to the site-specific analysis, most models simulate basin-scale temperature changes since the LGM well. SSs improve for some models with the basin-scale analysis, with values ranging from −0.25 to 0.93. Models still struggle to capture changes in evapotranspiration, with the same number of models calculating negative skill as the site-specific analysis and SSs of −2.54 to 0.22. For precipitation anomalies, basin-average skill decreases for all models, ranging from −0.58 to 0.20.

In all cases, the PMIP3 MIROC-ESM reflects conditions that are too cold and dry to match proxy values. This model performs the worst with respect to SS in every reconstructed variable from our proxy data using both site and basin averages. On average, it is 5° to 6° colder than the proxy reconstructions (fig. S2).

Overall, the models tend to capture temperature changes well but fail to accurately simulate evapotranspiration and precipitation. Poor model skill for precipitation and evaporation may be influenced by the lack of inclusion of pluvial lakes in LGM simulations. These lakes should substantially modify regional climate, and their exclusion could result in underestimation of localized moisture recycling and evaporation feedbacks, leading to discrepancies between models and proxy data. Simulations of hydroclimates would likely be improved by the inclusion of modern and ancient pluvial lake systems as boundary conditions in models to account for their potentially substantial role in modifying regional hydrology and climate.

Paleoclimatic lake-atmosphere interactions

Prior work has shown evidence of large precipitation increases during Heinrich Events within the southwestern United States (*4*, *32*, *38*). Between 24 and 22.3 ka, when our results show a 2.2 to 2.9 times modern increase in precipitation, there is a 150-m increase in lake level and associated changes in lake area at Lake Bonneville that are coeval with HS2 (~24 ka). Uranium and oxygen isotope data from deep-water cave carbonates in the Bonneville basin suggest a large degree of freshening in the basin, suggesting large increases in precipitation during HS2 (*32*). Increases in precipitation during HS2 have been proposed to have been felt as far south as New Mexico and Arizona, as supported by decreases in speleothem $\delta^{18}O$ during this time (*39*, *40*). Changes in the size and shape of the North American Ice Sheets and the resultant freshwater fluxes into the North Atlantic during Heinrich Events may have altered the strength and position

Downloaded from https://www.science.org at Brown University on January 25, 2026

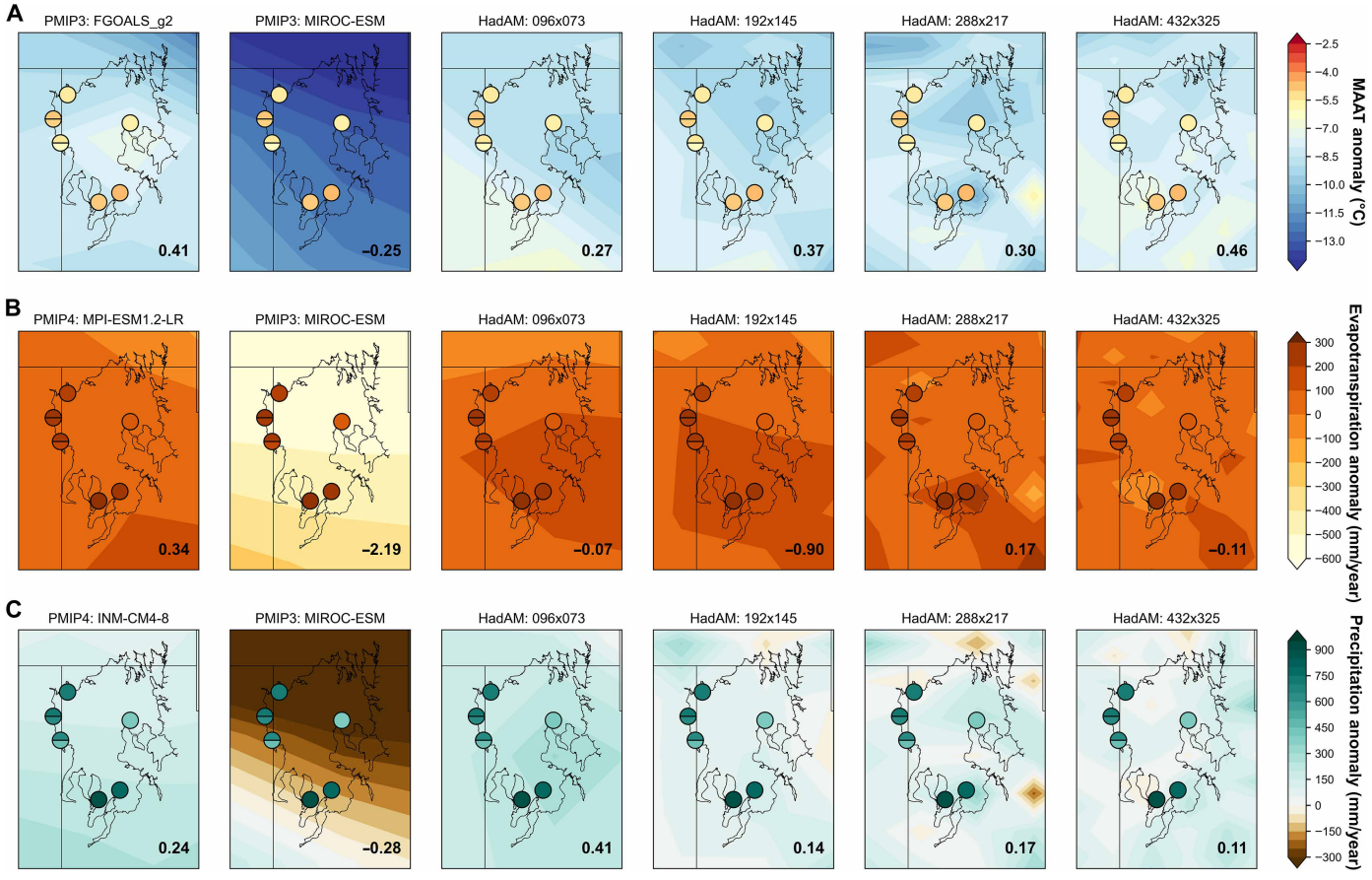

Fig. 4. Comparison of Δ47-derived hydroclimate variables at Lake Bonneville with PMIP3, PMIP4, and HadAM climate model simulations. Δ_{47} estimates of changes in MAAT (**A**), evapotranspiration (**B**), and precipitation (**C**) since the LGM compared to model simulations. Climate model SSs are shown (lower right; table S6) and calculated relative to LGM values (23 to 22 ka) derived from gastropods (whole circles) and gastropods and marls (split circles, top and bottom, respectively) (table S2). Panels from left to right display: PMIP3 and PMIP4 highest skill model, PMIP3 and PMIP4 lowest skill model, and HadAM skill ranging from lowest to highest resolution model.

of the subpolar and polar jet streams to deliver moisture into the continental interior during the winter (*4*, *32*).

While Lake Bonneville had a rapid ascent, the magnitude of the change in lake levels is not mirrored in the hydrograph from Lake Lahontan, the second-largest late Pleistocene lake in the Great Basin located ~400 km to the east, which only experienced a 40-m increase in the same interval (*3*, *41*). Given that these two basins are located at a similar latitude, an implied zonal trend could be explained if moisture transport from the North Pacific from a southward shifted jet was responsible for the rise in lake levels. Thus, given the gradient in precipitation between basins and the lower water $\delta^{18}O$ values recorded by these samples that are most consistent with winter precipitation, it is possible that Heinrich Event–driven changes in moisture delivery may be a contributor to increases in lake levels.

Because of the nature of these lakes being isolated from larger bodies of water and surrounded by land, a high thermal inertia causes the formation of mid-lake cloud bands known as lake effect clouds, with stratus types being the most common (*42*). Assuming that spatial distribution of stratus-type clouds follows the advancement of local glaciers, so will their radiative properties. In Stratus clouds, due to their ability to reflect high levels of incoming, shortwave radiation is known to cause a cooling effect at the surface (*43*), which would aid in maintaining cooler temperatures and lower evaporation levels. Stratus clouds are the favored cloud type for orographically induced precipitation through a phenomenon called the seeder-feeder mechanism (*44*, *45*). These conditions would be sufficient to explain decreased temperatures coupled with increased precipitation; however, there is no proxy for understanding past cloud distribution and thickness.

However, the contrast between the enhanced precipitation forcing observed within this study during the transgression of Lake Bonneville and lake level changes at Lake Lahontan suggests that both large-scale and localized feedback may have been influential in Bonneville's initial ascent. Since a similar rate of increase in lake levels is not reflected in records nearby, we hypothesize that lake-effect precipitation feedbacks paired with evaporative suppression may have been crucial in enhancing the magnitude of growth observed at Lake Bonneville during the early LGM (*46*).

At Lake Bonneville's maximum extent (~17.5 ka), it was similar in area and similar in depth to Lake Michigan and ~10 times greater in surface area and depth compared to the modern Great Salt Lake. Having a water body of that scale is likely to have influenced local hydroclimates, providing a water source for lake-effect precipitation. Regionally, modern lake effect precipitation occurs when the land-water temperature gradient exceeds 6°C, creating low-level convergence and promoting moisture uptake from the lake (*47*),

Downloaded from https://www.science.org at Brown University on January 25, 2026

Table 3. SS for PMIP3, PMIP4, and HadAM models based on comparison to clumped isotope–derived values. Model anomalies (LGM–preindustrial) were used for calculations. A SS of 1 indicates perfect proxy-model agreement. An SS of 0 indicates that the model and reference state perform equally well with respect to the null hypothesis of no change from the LGM to present. A negative SS indicates that the model error is greater than in the null hypothesis. An undefined SS (u.d.) occurs when the data-model agreement is closer than within the proxy errors (*36*, *37*).

Model	Temperature anomaly (°C)				Precipitation anomaly (mm/year)				Evaporation anomaly (mm/year)			
	Marl	Gastropods		Skill score	Marl	Gastropods		Skill score	Marl	Gastropods		Skill score
	Bonneville $\Delta T = -5.6$	Bonneville $\Delta T = -5.2$	Sevier $\Delta T = -6.0$		Bonneville $\Delta P = +413$	Bonneville $\Delta P = +524$	Sevier $\Delta P = +413$		Bonneville $\Delta E = +213$	Bonneville $\Delta E = +219$	Sevier $\Delta E = +210$	
PMIP3: NCAR-CCSM4	−10.2	−10.2	−9.7	0.17 (0.17)	50.7	50.7	40.3	0.09 (0.09)	−36	−36	−48	−0.19 (−0.19)
PMIP3: CNRM-CM5	−4.2	−4.2	−4.0	0.74 (0.78)	4.2	−9.0	−1.2	−0.01 (−0.01)	−27	−25	−10	−0.10 (−0.10)
PMIP3: COSMOS-ASO	−6.7	−6.7	−6.7	0.77 (0.82)	51.9	51.9	51.9	0.10 (0.10)	46	46	46	0.22 (0.23)
PMIP3: FGOALS_g2	−8.5	−6.9	−6.9	0.61 (0.64)	5.4	−302.3	−302.3	−0.58 (u.d.)	−119	−176	−176	−0.74 (−0.76)
PMIP3: GISS-E2-R	−5.0	−5.0	−6.0	0.93 (u.d.)	−22.4	−22.4	5.5	−0.04 (−0.04)	−30	−30	−260	−0.59 (−0.60)
PMIP3: IPSL-CM5A-LR	−8.0	−8.0	−7.7	0.55 (0.57)	−13.1	−13.1	144.8	−0.02 (−0.02)	−194	−194	22	−0.64 (−0.66)
PMIP3: MIROC-ESM	−11.8	−12.9	−12.9	−0.28 (−0.29)	−168.1	−301.7	−301.7	−0.63 (u.d.)	−507	−528	−528	−2.44 (−2.50)
PMIP3: MPI-ESM-P	−7.5	−7.5	−8.8	0.55 (0.57)	49.1	49.1	133.4	0.09 (0.09)	38	38	42	0.18 (0.19)
PMIP3: MRI-CGSM3	−6.2	−6.2	−6.2	0.85 (0.96)	−88.1	−88.1	−88.0	−0.19 (−0.19)	−147	−147	−219	−0.81 (−0.83)
PMIP4: AWI-ESM-1-1-LR	−5.6	−5.6	−6.1	0.92 (u.d.)	37.6	37.6	53.0	0.07 (0.07)	26	26	19	0.11 (0.11)
PMIP4: INM-CM4–8	−6.4	−6.4	−6.5	0.81 (0.89)	125.3	125.3	188.6	0.20 (0.20)	7	7	42	0.09 (0.09)
PMIP4: MIROC-ES2L	−7.1	−7.7	−7.7	0.61 (0.64)	47.8	−17.6	−17.6	−0.02 (−0.02)	−25	−135	−135	−0.48 (−0.50)
PMIP4: MPI-ESM1.2-LR	−5.7	−5.7	−6.5	0.89 (u.d.)	108.8	108.8	138.1	0.18 (0.18)	78	78	79	0.37 (0.38)
HadAM: 096x073	−9.2	−9.2	−9.2	0.32 (0.33)	302.9	302.9	302.9	0.14 (0.14)	181	181	181	−1.38 (−1.41)
HadAM: 192x145	−8.0	−8.7	−8.5	0.46 (0.47)	80.3	78.8	123.0	0.14 (0.14)	106	99	147	−1.38 (−1.41)
HadAM: 288x217	−9.4	−9.4	−10.6	0.21 (0.22)	112.0	112.0	338.2	0.10 (0.10)	113	113	285	0.01 (0.01)
HadAM: 432x325	−8.1	−8.1	−8.4	0.50 (0.52)	52.9	52.9	167.9	0.09 (0.09)	31	31	84	−0.15 (−0.16)

Downloaded from https://www.science.org at Brown University on January 25, 2026

with peaks in lake-effect precipitation between October and November and then again from March to April (*48*). At present, lake-effect precipitation accounts for up to 8% of regional precipitation and contributes to hydroclimate directly through precipitation over the lake and indirectly through snowpack that leads to runoff into the lake (*48*, *49*).

In addition to the thermally driven convergence, the complex regional terrain that surrounds the Great Salt Lake causes large-scale orographically forced convergence in the valleys, in turn funneling cold and dry air from the northwest that descends and warms, further enhancing precipitation in the downwind mountain ranges (*49*). The deposition of spits in Lake Bonneville suggest that winds had predominantly northeasterly or northwesterly flow in the LGM and deglaciation (*50*), which is the direction of flow needed for the formation of modern orographic lake effect precipitation in the Bonneville basin. Northwesterly winds would bring in cold, dry air from the ice sheet boundary into the Bonneville basin as the westerly storm track was diverted south, which could potentially influence moisture uptake and increase the frequency of orographically induced lake effect precipitation in Lake Bonneville.

As Lake Bonneville transgressed and lake area increased, air-water interactions over a larger surface area paired with the surrounding topography may have sustained an increased lake effect, where the thermal contrast between lake and land would promote moisture uptake and subsequent rainout due to orographic forcing (*2*). The lake-to-land temperature gradient would be greatest during the autumn months due to the depth and extent of the lake inhibiting complete ice coverage, allowing thermal lake-atmosphere interactions to develop and enhancing lake effect precipitation. Meteorological conditions conducive to lake effect precipitation during this interval may have allowed moisture generated from the lake to have fallen back as direct runoff or delayed snowmelt the following spring.

A modeling study by Hostetler and Giorgi (*46*) estimated that 32% of evaporation leaving Lake Bonneville was returned directly to the basin through moisture recycling at its maximum extent. However, our reconstructed water balance at the maximum extent indicates that evaporation decreased by ~600 mm/year relative to modern, while precipitation increased by only ~150 mm/year relative to modern. This imbalance suggests that, although precipitation did increase, it was the substantial reduction in evaporation, suggested by 3° to 4°C of regional cooling that played the dominant role in driving the lake to its highest elevation at ~17.5 ka.

Thermodynamic constraints on net water supply

To quantify the impact of hydrological cycle changes, particularly in determining the surplus of net water balance (i.e., precipitation minus evaporation, $P - E$), we apply a modified theory (*51*) derived from the Clausius-Clapeyron relationship. This theory has been applied to quantify the response of hydrological cycles during the LGM using climate model simulations (*52*). This relationship shows that temperature directly influences atmospheric water vapor content, with warmer conditions leading to increased water vapor in the atmosphere. Held and Soden (*51*) approximates the net water balance as a result of net exchange of water vapor content between the liquid and air and then further demonstrate that the ratio of net water balance anomalies, which is the water balance anomalies [$\delta(P - E)$, denoted by δ, representative of the difference between reconstructed and modern values] divided by modern $P - E$, exhibit a linear relationship with temperature anomalies (δT). This gives the equation $\delta(P - E)_{\text{paleo-modern}}/(P - E)_{\text{modern}} = \alpha\delta T$. The slope ($\alpha$) of this relationship is equal to the ratio of latent heat over the gas constant divided by the square of the modern MAAT in Kelvin, which is estimated to be 0.07 K^{-1}. As a result, the net water balance anomalies will rise by 7% when temperatures warm by 1°C.

Figure 5 shows the hydroclimatic parameters derived from clumped isotopes align with the theoretical predictions from the Clausius-Clapeyron scaling. This agreement implies that the hydrological cycle changes are fully controlled by temperature. Deviation in slope (away from 7%) would suggest that dynamical effects (e.g., changing storm tracks and atmospheric waves) had a discernable role in determining water supply. The data from shoreline tufas show a strong relationship between temperature suppression and net water supply ($r^2 = 0.78$), while results from gastropod and marl samples during the rapid transgression of the lake exhibit a weaker relationship ($r^2 = 0.37$). Thus, the results derived from tufas may suggest that the water surplus in Lake Bonneville primarily originated from a temperature reduction during glacial periods without substantial contributions from other dynamical factors. The weak relationship observed within gastropod and marl samples during the transgressive phase of the lake may indicate a larger influence of dynamic factors, consistent with the large (2.2 to 2.9× modern) precipitation increases reconstructed concurrent with rapid lake ascent during this period, which are difficult to explain from thermodynamics alone. These findings also highlight the value of the Clausius-Clapeyron relationship as a tool for understanding past hydrological changes and suggest that similar methods could be applied to other regions or time periods with limited but precise proxy data.

Water balance implications

In summary, clumped isotopes allow us to not only estimate past temperatures but quantify the impacts of temperature and evaporation on lake budgets and show their integral role in the growth and decline of Lake Bonneville during the LGM and subsequent

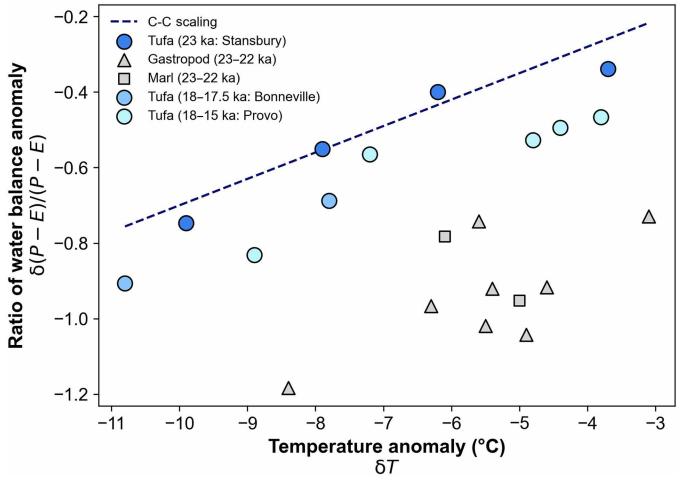

Fig. 5. Comparison of Δ_{47}-derived variables to predictions from the Clausius-Clapeyron scaling law. Results from tufas (blue filled circles) of different ages are in agreement with the Clausius-Clapeyron relationship (blue dashed line), indicating that water balance changes can simply be explained by temperature alone. Data from LGM gastropods (gray triangles) and marls (gray squares) during the transgressive phase of the lake deviate from this relationship and suggest a larger influence of dynamic factors.

Downloaded from https://www.science.org at Brown University on January 25, 2026

deglaciation. Results from this study show that evaporation rates decreased as lake levels at Lake Bonneville transgressed. We also quantify precipitation rates and show that there were two intervals with elevated precipitation relative to modern. During the early LGM, increased moisture delivery and moisture recycling within Lake Bonneville (i.e., lake effect precipitation) may have been integral contributors to the regional hydrologic budget since similarly large increases in lake area and extent were apparently not mirrored in nearby basins. Between 23 and 22 ka, during a transgression, and before the maxima, we hypothesize that cooling and associated evaporation suppression, paired with a combination of large-scale changes in precipitation driven by HS2, and localized, thermally and orographically driven lake-effect precipitation, together supported the notable ~150-m rise in shorelines of Lake Bonneville. During Heinrich Event 1, there was both a localized response and a larger-scale regional response, as evidenced by coeval pluvial maxima in the Great Basin during this time.

Overall, our results here suggest that reduced evaporation, combined with elevated regional precipitation at two to three times modern rates, contributed to the initial growth of Lake Bonneville and sustained it during a hydrologically open phase. Our results highlight the importance of temperature and thus evaporation as a direct driver of lakes, and the role of water recycling within basins, for understanding past and future hydrologic cycle responses to changing climate forcing, especially lakes with large surface areas in mid- to high-latitude settings. Analysis using the Clausius-Clapeyron relationship confirms that temperature reduction was the primary driver of the water surplus in Lake Bonneville. This result also provides strong evidence that thermodynamic factors, particularly temperature, are key determinants in shaping past lake hydrology, and not only dynamic processes such as storm tracks or jet meandering. A direction for future work is to address how changes in groundwater input and outflow from the lake may have also evolved and influenced surface and lake water budgets. In addition, while our tufa samples span both semi-restricted (Pilot Valley sub-basin) and open-basin (Great Salt Lake sub-basin) settings, it only represents one portion of the basin. Expanding tufa sampling for analysis across other regions could help assess spatial variability in lake water chemistry and reduce potential site-specific bias in interpretations of basin-wide hydrologic change.

We also note that this approach could be applied to other large lakes. Areas with complex terrain near large lakes similar to Lake Bonneville (e.g., Lake Lahontan in the Great Basin or Lake Tauca in the Altiplano) may also be sensitive to lake effect precipitation effects. We also suggest that the influence of lake-atmosphere interactions should be considered within paleohydrological reconstructions.

This work emphasized the central role that temperature has on water resources. In paleoclimatology, the reconstructions and insights reported here can help improve our understanding of how past changes in water availability shaped human and ecological systems, as the past hydrologic crises implied by the reconstructions likely had profound impacts on life and culture. This is also the case for the future. As the Great Salt Lake shrinks, a reduced lake effect is likely to accelerate the decline in modern lake levels, threatening water resources with human, ecosystem, and economic consequences in the region. Accurate model simulations of how much evaporation and precipitation rates will change as climate warms in the future, and local changes in lake water recycling, are critical for forecasting the extent of lakes as a key water resource.

MATERIALS AND METHODS

Sample collection

Field sample collection was carried out at sites within the Bonneville basin and Sevier sub-basin in October 2012 (Fig. 1 and Tables 1 and 2). Gastropods were collected from sand and gravel strata that correspond with littoral conditions. Based on sequence stratigraphic interpretations, the localities sampled record the initial transgression of the lake to a given shorezone. Gastropods were collected from lacustrine gravel directly underlying the Bonneville White Marl. The superposition of marl above the shell-bearing beds is laterally continuous across sites and records the transition from nearshore littoral to offshore lacustrine sedimentation. Samples of lacustrine tufa representing the Stansbury, Bonneville, and Provo shore zones were selected from the collection of Steve Nelson at Brigham Young University. These samples are from sites at the Pilot Valley sub-basin and Great Salt Lake sub-basin at the west end of the lake (Fig. 1). Oxygen and carbon stable isotope values were previously reported for these samples (*53*), but clumped isotope abundances were not measured. Tufa samples varied in texture. Some materials were porous and contained micrite and spar, while others were dense and lacked void spaces.

Sample preparation

Aragonitic gastropod shells were separated by taxa. Shells were broken into pieces, sonicated in Milli-Q deionized water until clean, dried overnight at 50°C, and powdered using a mortar and pestle. For a given study site, 4 to 10 individual gastropod shells were analyzed one to four times each, depending on sample limitations. Replicate analyses of individual shells served to test the reproducibility of isotope results. Individual gastropod shells represent short timescales; thus, analyses of multiple shells at a given site allowed for compilation of a statistically significant climatic signal.

Two to six individual blocks of marl were selected for clumped isotope analysis at each sampling site to ensure that reconstructed water temperatures encompassed the broadest interval of lake history. Sample blocks were disaggregated in Milli-Q water and poured through a 212-μm steel mesh filter to exclude particles coarser than fine sand (e.g., detrital clasts, charcoal, root, and biogenic shell fragments). Following sieving at 212 μm, the resultant slurry was allowed to settle for 5 to 10 min. The residue coming out of suspension was isolated by pouring the slurry into a second beaker. This process was repeated until virtually no settling occurred. The final suspension was treated with dilute hydrogen peroxide (1.5 to 3%) for 20 to 60 minutes to remove residual organic material (*54*). Carbonate was collected on 0.45-μm cellulose nitrate filter membranes and dried overnight at 50°C.

Tufas and cements were cut perpendicular to laminae. Areas containing spar, or evidence of regrowth, were selected against. Powders were extracted by crushing rock chips to fine sand grain size, following methodology in (*53*). Powdered tufa samples were reacted in 3% H_2O_2 for 60 min to remove organic materials (*54*). Following peroxide treatment, samples were rinsed in Milli-Q deionized water and dried for 12 hours at 50°C. Cleaned powders were weighed out in 5- to 15-mg increments, depending on carbonate content and instrument sensitivity at the time of analysis.

Analytical procedure for stable and clumped isotopes

Samples were reacted for 20 min on a 90°C common phosphoric acid bath system in the Tripati Lab at University of California, Los Angeles. For samples containing greater than 90% carbonate

Downloaded from https://www.science.org at Brown University on January 25, 2026

(i.e., gastropod shell), sufficient CO_2 gas was obtained from acid digestion of 5 to 10 mg of material. In the case of samples with lower carbonate content (e.g., carbonate muds), 10 to 50 mg of samples were reacted to generate sufficient CO_2 gas. Samples were run for at least three replicates, unless there was insufficient material for analysis. The acid bath was maintained at constant temperature through use of a cylindrical heating block with a thermocouple feedback system. The temperature of the acid bath was physically measured with a glass thermometer daily and found to be at 90°C. CO_2 was cryogenically purified using an automated vacuum line that was modeled on a system at the California Institute of Technology (*55*). Organic compounds were removed with a Porapak column installed on a Thermo Trace GC Ultra gas chromatograph. $\delta^{13}C$, $\delta^{18}O$, Δ_{47}, and Δ_{48} were determined using a Thermo 253 Gas Source isotope ratio mass spectrometer.

During 2013 and the first half of 2014, samples were run for eight acquisition cycles consisting of 10 measurements of sample and reference gas. During the latter half of 2014 and onward, samples were run for nine acquisition cycles consisting of 10 measurements of sample and reference gas. During each acquisition, sample gas voltages were compared to high-purity Oztech brand CO_2 reference gas [$\delta^{18}O = 25.03‰$ V-SMOW, $\delta^{13}C = -3.60‰$ Vienna Pee Dee Belemnite (V-PDB)]. CO_2 gas standards and carbonate standards of known isotopic compositions were run every four to five analyses. To account for mineral digestion in a common acid bath to produce CO_2 to determine $\delta^{18}O$ values for carbonate samples, a fractionation factor of 1.007954 for calcite and 1.00854 for aragonite was applied, following (*56*) and (*57*), respectively.

Data were processed using the Easotope software using the brand parameter set (*58*, *59*). Results were normalized following the absolute reference frame correction and standardization process (*60*). Signal interference due to electron backscattering in the source of the mass spectrometer was quantified and corrected for using equilibrated gases with two different bulk isotopic signatures at two different temperatures (25° and 1000°C) and ETH-1 and ETH-2 from the ETH suite of standards (*61*). Aliquots of gas were cryogenically purified on a manual vacuum line system and collected in borosilicate breakseal tubes. Changes in slope of δ_{47} versus Δ_{47} were attributed to shifting conditions in the source of the mass spectrometer and occasionally to the presence of organic contaminants. Samples were strictly run during periods of time in which the calculated slopes of regressions, relating δ_{47} versus Δ_{47}, did not change. ETH-1 to ETH-3 along with internal standards were used to create an empirical transfer function to convert values to the Intercarb Carbon Dioxide Equilibrium Scale (I-CDES) to calculate the final Δ_{47} value (*61*, *62*). Δ_{47} values for sample and standard runs are presented in tables S1 and S3.

Elevation and age control

Sample altitude was corrected for using the Currey equation (*63*), where Z_a is the rebound-free adjusted altitude, Z_r is the modern mapped altitude of the sample, Z_b is the local altitude of the Bonneville shoreline, and 1552 and 1200 are the average unrebounded altitude of Bonneville shoreline and basin floor altitude at the beginning of the Bonneville lake cycle, respectively, and all elevations are in meters

$$Z_a = Z_r - \left[\frac{(Z_r - 1200)}{(Z_b - 1200)}\right] \times \left[Z_b - 1552\right]$$

Ages for samples were then assigned by interpolation along the updated lake hydrograph of Oviatt and Pedone (*7*) (Fig. 2E) using the rebound-adjusted altitude. The updated hydrograph of Oviatt and Pedone (*7*), based on U-Th and radiocarbon-dated microbialites, revises the earlier framework of Oviatt (*9*) by excluding mollusk dates (due to large geologic uncertainties and reservoir effects) and treating wood and charcoal as maximum limiting ages rather than closely constraining the timing of lake transgression. Ages for the Bonneville and Provo shoreline tufas are determined by interpolation, with additional constraints from prior work. The age of the Bonneville shoreline is further constrained by recent work from Oviatt *et al.* (*8*), which estimates an age of ~17.5 ± 0.5 ka based on limiting radiocarbon ages from deposits beneath the shoreline and consistency with inferred long-term transgression rates. For the Provo shoreline, which may reflect multigenerational tufa formation between ~18 and 15 ka (*9*), we use ~16.5 ka as a representative midpoint. Ages for the gastropod and marl samples were also determined by interpolation along the updated hydrograph, with additional constraints from prior work. The gastropod-bearing beds underlying the marl samples have radiometric constraints from equivalent horizons dated at or near the sampled sites [(*64*) and references therein], providing independent chronologic control consistent with deposition during the transgressive phase of Lake Bonneville.

We acknowledge that absolute age estimates based on hydrograph interpolation carry inherent uncertainty; however, the relative timing among major lake phases—pre-Bonneville transgression, Bonneville highstand, and Provo regression—is well constrained and provides a robust framework for our paleohydrological interpretations.

Δ_{47} temperature dependence

The clumped isotope value (Δ_{47}) can be related to the temperature of ambient waters at the time of mineralization, where lower temperatures are associated with a greater abundance of ^{13}C—^{18}O bonds (*26*, *65*, *66*). Clumped isotope measurements (Δ_{47}) were converted to water temperatures using the material-specific calibrations of Arnold *et al.* (*67*), with the following equations used for each type of carbonate

$$\Delta_{47}\,(\text{gastropods}) = (0.0371 \pm 0.004) \times 10^6/T^2 + (0.174 \pm 0.051)$$

$$\Delta_{47}\,(\text{tufas}) = (0.0345 \pm 0.007) \times 10^6/T^2 + (0.216 \pm 0.080)$$

$$\Delta_{47}\,(\text{marls}) = (0.0462 \pm 0.007) \times 10^6/T^2 + (0.084 \pm 0.089)$$

Calculation of water $\delta^{18}O$

Lake water $\delta^{18}O$ ($\delta^{18}O_{water}$) values were calculated using estimations of mineralization temperatures and $\delta^{18}O_{carbonate}$ values from clumped isotope analysis, in concert with using mineral specific fractionation values for calcite (*68*) and aragonite (*57*). Reconstructions in this work were reported with an ice-volume correction applied to account for enrichment of ^{18}O in the glacial ocean during the LGM (*26*). This approach was chosen because the samples in this study span both the LGM and the deglacial period, and meltwater input from ice sheets likely altered ocean $\delta^{18}O$ composition over time, necessitating consideration of temporal variability in the correction. Thus, we use the approach outlined in (*26*) to constrain the composition of the global ocean through the late Pleistocene. In this

Downloaded from https://www.science.org at Brown University on January 25, 2026

approach, a $\Delta\delta^{18}O$-Δsea level relationship of ~0.08‰/meter sea level change is applied using the sea level change estimates derived from (*69*).

Mean annual air temperature

Evaluation of seasonal relationships between air and water temperature in modern lakes indicate that lake surface temperature will closely match air temperature (*25*, *70*). To reconstruct air temperature at study sites, transfer functions using Model 4 in (*25*) were applied to relate water surface temperature, latitude, and elevation to MAAT, assuming a seasonal dependence of carbonate formation. Gastropod shells were assigned April–June transfer functions due to primary shell formation occurring in unison with peak photosynthetic activity in the mid to high latitudes (*71*). The calcification of tufa is dependent on photosynthetic activity, wave action, and evaporation and thus was assigned a larger growth season (April–October) for our analyses (*53*, *72*). Because of the temperature dependence of evaporation promoting carbonate saturation state within the lake, marls in this study were assigned a June–August transfer function to represent the warmest interval of the year (*70*, *73*). Site-specific modern MAATs used to calculate anomalies are in table S2.

Evaporation modeling

We reconstructed estimates of annual evaporation (E_L) using the modified Penman equation from Linacre (*74*). This method has inputs of MAAT (T), elevation (z), latitude (L), wind speed (u), and dew point temperature (T_d).

$$E_L = \left[0.015 + 4\times10^{-4}\ T + 10^{-6}z\right] \times \left[\frac{480\,(T+0.006z)}{(84-L)} - 40 + 2.3u\left(T-T_d\right)\right]$$

MAAT was calculated using clumped isotope estimates of water temperature applied to transfer functions in (*25*). Dew point (T_d) temperature and wind speed (u) was estimated by using modern reanalysis data over the modern Bonneville basin and assumed to be similar to modern during the LGM. T_d values for the LGM were assumed to change by magnitudes equal to shifts in air temperature from present (*20*, *75*). Average pan evaporation rates (1443 mm/year) were calculated using 13 modern sites in the Bonneville basin (table S4) (*31*). Average modern lake evaporation rates were estimated using a pan coefficient of 0.9 from (*30*).

Precipitation modeling

Estimates of precipitation were constrained using the modeling framework described within (*19*). This method combines $\delta^{18}O$ isotope mass balance, time-varying water balance, and basin hypsometry to create a function to estimate annual precipitation rates (*19*, *20*)

$$P = \frac{E_L}{\left(1+\frac{k_{run}}{HI}\right)} \times \frac{\left(\delta^{18}O_E - \delta^{18}O_L\right)}{\left(\delta^{18}O_W - \delta^{18}O_L\right)}$$

Lake evaporation (E_L) is estimated using the equation in the prior section. Basin hypsometry is included through the hydrologic index (HI), which is the ratio of lake area to tributary area. The oxygen isotopic composition of the lake ($\delta^{18}O_L$) was determined using clumped isotope–derived estimates of temperature and measured oxygen composition of the carbonate. The evaporating water vapor ($\delta^{18}O_E$) is estimated using the evaporation model from (*76*). The average composition of the incoming meteoric water ($\delta^{18}O_W$) was estimated using modern values for all sample sites (table S5; -13.3 ± 1.3‰ V-SMOW) and is interpolated to pre-rebound elevations and corrected for LGM ^{18}O enrichment (*26*, *77*, *78*). To account for the nonlinear response of runoff to changes in precipitation, a Budyko framework is used to estimate k_{run} (*19*, *34*, *79*)

$$1 - k_{run} = \frac{ET}{P} = 1 + \frac{E_P}{P} - \left[1 + \left(\frac{E_P}{P}\right)^{\omega}\right]^{1/\omega}$$

Potential evapotranspiration (E_P) is assumed to be equal to lake evaporation (E_L), and ω is the Budyko landscape parameter, which integrates the hydrologic properties of a basin. To constrain hydroclimatic variables, a Monte Carlo simulation with 2500 iterations is used to determine find the roots of the equations for precipitation and runoff, with all variables sampled from a normal distribution using the mean and SD for each variable (*19*), with the exception of ω, which is sampled from a skewed gamma distribution derived from the MOPEX dataset and calibrated from the conterminous United States (*79*). Factor change in precipitation rates is calculated using the basin-average 30-year normal modern value of 344 mm/year (*29*).

Evapotranspiration and weighted evaporation modeling

To allow our results to be comparable with land-surface evapotranspiration rates from climate model output, we calculate evapotranspiration (ET) using precipitation (P) and the runoff coefficient (k_{run}) derived in our hydroclimate modeling using the following equation

$$ET = P \times \left(1 - k_{run}\right)$$

We calculate a weighted evaporation (WE) rate to scale lake evaporation (E_L) occurring over the lake area (A_L) and evapotranspiration occurring in the tributary area (A_T) using the following equation

$$WE = \frac{\left(P - K_{run} \times A_L\right) + E_L \times A_L}{A_T + A_L}$$

Climate model evaluation

We compare the results derived in this study to climate model output from the PMIP3 and PMIP4 models and output from the HadAM at four different resolutions, varying from low resolution (2.5° × 3.75°) to high (0.6° × 0.8°) resolution. For PMIP models, we use near-surface air temperature (tas), precipitation (pr), and evapotranspiration (evspbl) climatological monthly means to compare to our data. For the HadAM models, we use near-surface air temperature (temp_mm_srf), precipitation (precip_mm_srf), and evapotranspiration (totalevap) annual means to compare to our data. Temperature, precipitation, and evapotranspiration anomalies were compared to results from models and evaluated using the SS metric (*36*, *37*), where m_i is the results from the model, n_i is the reference state (assumed to be zero or no change between the LGM and present), and o_i and e_i are the observations and their respective errors (derived from clumped isotope analysis)

$$SS\ (\text{without proxy error}) = 1 - \sqrt{\frac{\Sigma\left(m_i - o_i\right)^2}{\Sigma\left(n_i - o_i\right)^2}}$$

Downloaded from https://www.science.org at Brown University on January 25, 2026

$$\mathrm{SS}\left(\text{with proxy error}\right) = 1 - \sqrt{\frac{\Sigma\left(m_i - o_i\right)^2 - \Sigma\left(e_i\right)^2}{\Sigma\left(n_i - o_i\right)^2 - \Sigma\left(e_i\right)^2}}$$

We calculate SS using both equations above, with the SS equation without proxy error to assess general proxy-model agreement when the SS is undefined.

Supplementary Materials

This PDF file includes:

Supplementary Text
Figs. S1 to S10
Tables S1 to S8
References

REFERENCES

1. G. K. Gilbert, "Lake Bonneville" (Report 1, U.S. Geological Survey, 1890); https://doi.org/10.3133/m1.
2. S. W. Hostetler, F. Giorgi, G. T. Bates, P. J. Bartlein, Lake-atmosphere feedbacks associated with Paleolakes Bonneville and Lahontan. *Science* **263**, 665–668 (1994).
3. M. C. Reheis, K. D. Adams, C. G. Oviatt, S. N. Bacon, Pluvial lakes in the great basin of the Western United States—A view from the outcrop. *Quat. Sci. Rev.* **97**, 33–57 (2014).
4. D. McGee, E. Moreno-Chamarro, J. Marshall, E. D. Galbraith, Western U.S. lake expansions during Heinrich stadials linked to Pacific Hadley circulation. *Sci. Adv.* **4**, eaav0118 (2018).
5. K. D. Adams, B. G. Bills, Chapter 8 - Isostatic rebound and palinspastic restoration of the Bonneville and Provo shorelines in the Bonneville Basin, UT, NV, and ID. *Dev. Earth Surf. Process.* **20**, 145–164 (2016).
6. T. Goebel, Pre-Archaic and early Archaic technological activities at Bonneville Estates Rockshelter: A first look at the lithic artifact record. (Univ. of Utah Press, 2007), pp. 156–184.
7. C. G. Oviatt, V. A. Pedone, Chronology of the early transgressive phase of Lake Bonneville. *Quat. Res.* **121**, 32–39 (2024).
8. C. G. Oviatt, GK Gilbert and the Bonneville shoreline. *GIW* **7**, 300–320 (2020).
9. C. G. Oviatt, Chronology of Lake Bonneville, 30,000 to 10,000 yr B.P. *Quat. Sci. Rev.* **110**, 166–171 (2015).
10. C. G. Oviatt, D. Craig Young, D. Duke, The Currey cycle of great salt lake: An early younger dryas lake in the Bonneville basin, Utah, USA. *J. Quat. Sci.* **39**, 932–945 (2024).
11. T. Arnow, D. W. Stephens, "Hydrologic characteristics of the Great Salt Lake, Utah: 1847–1986" (Report 2332, U.S. Geological Survey, 1990); https://doi.org/10.3133/wsp2332.
12. E. Antevs, *The Great Basin, with Emphasis on Glacial and Postglacial Times: Climatic Changes and Pre-White Man. Ill.* (University of Utah, 1948).
13. J. S. Munroe, B. J. Laabs, Temporal correspondence between pluvial lake highstands in the southwestern US and Heinrich Event 1. *J. Quat. Sci.* **28**, 49–58 (2013).
14. P. U. Clark, P. J. Bartlein, Correlation of late Pleistocene glaciation in the Western United States with North Atlantic Heinrich events. *Geology* **23**, 483–486 (1995).
15. B. J. Quirk, J. R. Moore, B. J. Laabs, M. A. Plummer, M. W. Caffee, Latest Pleistocene glacial and climate history of the Wasatch Range, Utah. *Quat. Sci. Rev.* **238**, 106313 (2020).
16. B. J. Quirk, J. R. Moore, B. J. Laabs, M. W. Caffee, M. A. Plummer, Termination II, last glacial maximum, and lateglacial chronologies and paleoclimate from Big Cottonwood Canyon, Wasatch Mountains, Utah. *GSA Bulletin* **130**, 1889–1902 (2018).
17. J. M. Lora, J. L. Mitchell, A. E. Tripati, Abrupt reorganization of North Pacific and western North American climate during the last deglaciation. *Geophys. Res. Lett.* **43**, 11796–11804 (2016).
18. M. Lyle, L. Heusser, C. Ravelo, M. Yamamoto, J. Barron, N. S. Diffenbaugh, T. Herbert, D. Andreasen, Out of the tropics: The pacific, great basin lakes, and late pleistocene water cycle in the Western United States. *Science* **337**, 1629–1633 (2012).
19. L. Santi, A. J. Arnold, D. E. Ibarra, C. A. Whicker, J. A. Mering, R. B. Lomarda, J. M. Lora, A. Tripati, Clumped isotope constraints on changes in latest Pleistocene hydroclimate in the northwestern Great Basin: Lake Surprise, California. *GSA Bulletin* **132**, 2669–2683 (2020).
20. D. E. Ibarra, A. E. Egger, K. L. Weaver, C. R. Harris, K. Maher, Rise and fall of late Pleistocene pluvial lakes in response to reduced evaporation and precipitation: Evidence from Lake Surprise, California. *GSA Bulletin* **126**, 1387–1415 (2014).
21. D. S. Kaufman, Amino acid paleothermometry of Quaternary ostracodes from the Bonneville Basin, Utah. *Quat. Sci. Rev.* **22**, 899–914 (2003).
22. F. Cheng, C. Garzione, X. Li, U. Salzmann, F. Schwarz, A. M. Haywood, J. Tindall, J. Nie, L. Li, L. Wang, Alpine permafrost could account for a quarter of thawed carbon based on Plio-Pleistocene paleoclimate analogue. *Nat. Commun.* **13**, 1329 (2022).
23. H. Li, X. Liu, A. Arnold, B. Elliott, R. Flores, A. M. Kelley, A. Tripati, Mass 47 clumped isotope signatures in modern lacustrine authigenic carbonates in Western China and other regions and implications for paleotemperature and paleoelevation reconstructions. *Earth Planet. Sci. Lett.* **562**, 116840 (2021).
24. V. A. Petryshyn, D. Lim, B. L. Laval, A. Brady, G. Slater, A. K. Tripati, Reconstruction of limnology and microbialite formation conditions from carbonate clumped isotope thermometry. *Geobiology* **13**, 53–67 (2015).
25. A. Terrazas, N. Hwangbo, A. J. Arnold, R. N. Ulrich, A. Tripati, Seasonal lake-to-air temperature transfer functions derived from an analysis of 1395 modern lakes: A tool for reconstructing air temperature from proxy-derived lake water temperature. *Depos. Record* **11**, 718–738 (2025).
26. A. K. Tripati, S. Sahany, D. Pittman, R. A. Eagle, J. D. Neelin, J. L. Mitchell, L. Beaufort, Modern and glacial tropical snowlines controlled by sea surface temperature and atmospheric mixing. *Nat. Geosci.* **7**, 205–209 (2014).
27. D. B. Madsen, D. Rhode, D. K. Grayson, J. M. Broughton, S. D. Livingston, J. Hunt, J. Quade, D. N. Schmitt, M. W. Shaver, Late quaternary environmental change in the Bonneville basin, Western USA. *Palaeogeogr. Palaeoclimatol. Palaeoecol.* **167**, 243–271 (2001).
28. R. S. Harbert, K. C. Nixon, Quantitative late quaternary climate reconstruction from plant macrofossil communities in Western North America. *Open Quat.* **4**, 8 (2018).
29. PRISM Climate Group (Oregon State University, 2024); https://prism.oregonstate.edu.
30. Y. Matsubara, A. D. Howard, A spatially explicit model of runoff, evaporation, and lake extent: Application to modern and late Pleistocene lakes in the Great Basin region, Western United States. *Water Resour. Res.* **45**, W06425 (2009).
31. Western Regional Climate Center. Average Pan Evaporation Comparison Table (2023); https://wrcc.dri.edu/Climate/comp_table_show.php?stype=pan_evap_avg.
32. D. McGee, J. Quade, R. L. Edwards, W. S. Broecker, H. Cheng, P. W. Reiners, N. Evenson, Lacustrine cave carbonates: Novel archives of paleohydrologic change in the Bonneville Basin (Utah, USA). *Earth Planet. Sci. Lett.* **351–352**, 182–194 (2012).
33. J. M. Welker, ENSO effects on δ18O, δ2H and d-excess values in precipitation across the U.S. using a high-density, long-term network (USNIP). *Rapid Commun. Mass Spectrom.* **26**, 1893–1898 (2012).
34. D. E. Ibarra, J. L. Oster, M. J. Winnick, J. K. C. Rugenstein, M. Byrne, C. P. Chamberlain, Lake area constraints on past hydroclimate in the western United States: Application to Pleistocene Lake Bonneville. EarthArXiv [Preprint] 2018); https://doi.org/10.31223/osf.io/rk5pe.
35. B. K. Belanger, W. H. Amidon, B. J. C. Laabs, J. S. Munroe, B. J. Quirk, Modelling climate constraints on the formation of pluvial Lake Bonneville in the Great Basin, United States. *J. Quat. Sci.* **37**, 478–488 (2022).
36. J. C. Hargreaves, J. D. Annan, R. Ohgaito, A. Paul, A. Abe-Ouchi, Skill and reliability of climate model ensembles at the Last Glacial Maximum and mid-Holocene. *Climate Past* **9**, 811–823 (2013).
37. J. M. Lora, D. E. Ibarra, The North American hydrologic cycle through the last deglaciation. *Quat. Sci. Rev.* **226**, 105991 (2019).
38. C. G. Oviatt, Lake Bonneville fluctuations and global climate change. *Geology* **25**, 155–158 (1997).
39. J. D. Wagner, J. E. Cole, J. W. Beck, P. J. Patchett, G. M. Henderson, H. R. Barnett, Moisture variability in the southwestern United States linked to abrupt glacial climate change. *Nat. Geosci.* **3**, 110–113 (2010).
40. Y. Asmerom, V. J. Polyak, S. J. Burns, Variable winter moisture in the southwestern United States linked to rapid glacial climate shifts. *Nat. Geosci.* **3**, 114–117 (2010).
41. L. V. Benson, J. P. Smoot, S. P. Lund, S. A. Mensing, F. F. Foit Jr., R. O. Rye, Insights from a synthesis of old and new climate-proxy data from the Pyramid and Winnemucca lake basins for the period 48 to 11.5 cal ka. *Quat. Int.* **310**, 62–82 (2013).
42. M. R. Hjelmfelt, R. R. Braham, Numerical simulation of the airflow over Lake Michigan for a Major lake-effect snow event. *Mon. Weather Rev.* **111**, 205–219 (1983).
43. S. H. Schneider, Cloudiness as a global climatic feedback mechanism: The effects on the radiation balance and surface temperature of variations in cloudiness. *J. Atmos. Sci.* **29**, 1413–1422 (1972).
44. M. J. Bader, W. T. Roach, Orographic rainfall in warm sectors of depressions. *Q. J. Roy. Meteorol. Soc.* **103**, 269–280 (1977).
45. Z. Dedekind, U. Proske, S. Ferrachat, U. Lohmann, D. Neubauer, Simulating the seeder–feeder impacts on cloud ice and precipitation over the Alps. *Atmos. Chem. Phys.* **24**, 5389–5404 (2024).
46. S. W. Hostetler, F. Giorgi, Use of a regional atmospheric model to simulate lake-atmosphere feedbacks associated with Pleistocene Lakes Lahontan and Bonneville. *Clim. Dyn.* **7**, 39–44 (1992).
47. W. J. Steenburgh, S. F. Halvorson, D. J. Onton, Climatology of lake-effect snowstorms of the great salt lake. *Mon. Weather Rev.* **128**, 709–727 (2000).
48. K. N. Yeager, W. J. Steenburgh, T. I. Alcott, Contributions of lake-effect periods to the cool-season hydroclimate of the great salt Lake Basin. *J. Appl. Meteorol. Climatol.* **52**, 341–362 (2013).
49. T. I. Alcott, W. J. Steenburgh, Orographic influences on a great salt lake–effect snowstorm. *Mon. Weather Rev.* **141**, 2432–2450 (2013).

Downloaded from https://www.science.org at Brown University on January 25, 2026

50. P. W. Jewell, Morphology and paleoclimatic significance of Pleistocene Lake Bonneville spits. *Quatern. Res.* **68**, 421–430 (2007).
51. I. M. Held, B. J. Soden, Robust responses of the hydrological cycle to global warming. *J. Climate* **19**, 5686–5699 (2006).
52. W. R. Boos, Thermodynamic scaling of the hydrological cycle of the last glacial maximum. *J. Clim.* **25**, 992–1006 (2012).
53. S. T. Nelson, M. J. Wood, A. L. Mayo, D. G. Tingey, D. Eggett, Shoreline tufa and tufaglomerate from Pleistocene Lake Bonneville, Utah, USA: Stable isotopic and mineralogical records of lake conditions, processes, and climate. *J. Quat. Sci.* **20**, 3–19 (2005).
54. R. A. Eagle, C. Risi, J. L. Mitchell, J. M. Eiler, U. Seibt, J. D. Neelin, G. Li, A. K. Tripati, High regional climate sensitivity over continental China constrained by glacial-recent changes in temperature and the hydrological cycle. *Proc. Natl. Acad. Sci. U.S.A.* **110**, 8813–8818 (2013).
55. B. H. Passey, N. E. Levin, T. E. Cerling, F. H. Brown, J. M. Eiler, High-temperature environments of human evolution in East Africa based on bond ordering in paleosol carbonates. *Proc. Natl. Acad. Sci. U.S.A.* **107**, 11245–11249 (2010).
56. P. K. Swart, S. J. Burns, J. J. Leder, Fractionation of the stable isotopes of oxygen and carbon in carbon dioxide during the reaction of calcite with phosphoric acid as a function of temperature and technique. *Chem. Geol.* **86**, 89–96 (1991).
57. S.-T. Kim, J. R. O'Neil, C. Hillaire-Marcel, A. Mucci, Oxygen isotope fractionation between synthetic aragonite and water: Influence of temperature and Mg2+ concentration. *Geochim. Cosmochim. Acta* **71**, 4704–4715 (2007).
58. W. A. Brand, S. S. Assonov, T. B. Coplen, Correction for the 17O interference in δ(13C) measurements when analyzing CO2 with stable isotope mass spectrometry (IUPAC Technical Report). *Pure Appl. Chem.* **82**, 1719–1733 (2010).
59. C. M. John, D. Bowen, Community software for challenging isotope analysis: First applications of 'Easotope' to clumped isotopes. *Rapid Commun. Mass Spectrom.* **30**, 2285–2300 (2016).
60. K. J. Dennis, H. P. Affek, B. H. Passey, D. P. Schrag, J. M. Eiler, Defining an absolute reference frame for 'clumped' isotope studies of CO2. *Geochim. Cosmochim. Acta* **75**, 7117–7131 (2011).
61. S. M. Bernasconi, M. Daëron, K. D. Bergmann, M. Bonifacie, A. N. Meckler, H. P. Affek, N. Anderson, D. Bajnai, E. Barkan, E. Beverly, D. Blamart, L. Burgener, D. Calmels, C. Chaduteau, M. Clog, B. Davidheiser-Kroll, A. Davies, F. Dux, J. Eiler, B. Elliott, A. C. Fetrow, J. Fiebig, S. Goldberg, M. Hermoso, K. W. Huntington, E. Hyland, M. Ingalls, M. Jaggi, C. M. John, A. B. Jost, S. Katz, J. Kelson, T. Kluge, I. J. Kocken, A. Laskar, T. J. Leutert, D. Liang, J. Lucarelli, T. J. Mackey, X. Mangenot, N. Meinicke, S. E. Modestou, I. A. Müller, S. Murray, A. Neary, N. Packard, B. H. Passey, E. Pelletier, S. Petersen, A. Piasecki, A. Schauer, K. E. Snell, P. K. Swart, A. Tripati, D. Upadhyay, T. Vennemann, I. Winkelstern, D. Yarian, N. Yoshida, N. Zhang, M. Ziegler, InterCarb: A community effort to improve interlaboratory standardization of the carbonate clumped isotope thermometer using carbonate standards. *Geochem. Geophys. Geosyst.* **22**, e2020GC009588 (2021).
62. J. K. Lucarelli, H. M. Carroll, R. N. Ulrich, B. M. Elliott, T. B. Coplen, R. A. Eagle, A. Tripati, Equilibrated Gas and Carbonate Standard-Derived Dual (Δ47 and Δ48) Clumped Isotope Values. *Geochem. Geophys. Geosyst.* **24**, e2022GC010458 (2023).
63. C. G. Oviatt, D. R. Currey, D. Sack, Radiocarbon chronology of Lake Bonneville, Eastern Great Basin, USA. *Palaeogeogr. Palaeoclimatol. Palaeoecol.* **99**, 225–241 (1992).
64. J. A. Mering, "New constraints on water temperature at lake bonneville from carbonate clumped isotopes," MS thesis, University of California, Los Angeles (2015).
65. R. A. Eagle, J. M. Eiler, A. K. Tripati, J. B. Ries, P. S. Freitas, C. Hiebenthal, A. D. Wanamaker, M. Taviani, M. Elliot, S. Marenssi, K. Nakamura, P. Ramirez, K. Roy, The influence of temperature and seawater carbonate saturation state on ^{13}C–^{18}O bond ordering in bivalve mollusks. *Biogeosciences* **10**, 4591–4606 (2013).
66. P. Ghosh, J. Adkins, H. Affek, B. Balta, W. Guo, E. A. Schauble, D. Schrag, J. M. Eiler, ^{13}C–^{18}O bonds in carbonate minerals: A new kind of paleothermometer. *Geochim. Cosmochim. Acta* **70**, 1439–1456 (2006).
67. A. Arnold, J. Mering, L. Chari, C. Román-Palacios, H. Li, V. Petrys hyn, B. Mitsunaga, B. Elliott, J. Wilson, J. Lucarelli, R. Boch, D. Ibarra, L. Li, M. Fan, D. Kaufman, A. Cohen, R. Dunbar, J. Russell, S. Lalonde, P. D. Roy, M. Dietzel, X. Liu, F. Chang, R. A. Eagle, A. Tripati, Comparative clumped isotope temperature relationships in freshwater carbonates. *Depos. Record* **11**, 418–443 (2025).
68. S.-T. Kim, J. R. O'Neil, Equilibrium and nonequilibrium oxygen isotope effects in synthetic carbonates. *Geochim. Cosmochim. Acta* **61**, 3461–3475 (1997).
69. K. Lambeck, J. Chappell, Sea level change through the last glacial cycle. *Science* **292**, 679–686 (2001).
70. M. T. Hren, N. D. Sheldon, Temporal variations in lake water temperature: Paleoenvironmental implications of lake carbonate $\delta^{18}O$ and temperature records. *Earth Planet. Sci. Lett.* **337**, 77–84 (2012).
71. E. A. Versteegh, H. B. Vonhof, S. R. Troelstra, R. J. Kaandorp, D. Kroon, Seasonally resolved growth of freshwater bivalves determined by oxygen and carbon isotope shell chemistry. *Geochem. Geophys. Geosyst.* **11**, Q08022 (2010).
72. A. Felton, P. W. Jewell, M. Chan, D. Currey, Controls of Tufa Development in Pleistocene Lake Bonneville, Utah. *J. Geol.* **114**, 377–389 (2006).
73. V. A. Petryshyn, M. Juarez Rivera, H. Agić, C. M. Frantz, F. A. Corsetti, A. E. Tripati, Stromatolites in Walker Lake (Nevada, Great Basin, USA) record climate and lake level changes ~ 35,000 years ago. *Palaeogeogr. Palaeoclimatol. Palaeoecol.* **451**, 140–151 (2016).
74. E. T. Linacre, Data-sparse estimation of lake evaporation, using a simplified Penman equation. *Agric. For. Meteorol.* **64**, 237–256 (1993).
75. M. D. Jones, C. N. Roberts, M. J. Leng, Quantifying climatic change through the last glacial–interglacial transition based on lake isotope palaeohydrology from central Turkey. *Quatern. Res.* **67**, 463–473 (2007).
76. H. Craig, L. I. Gordon, Deuterium and oxygen 18 variations in the ocean and the marine atmosphere. (1965).
77. G. J. Bowen, The Online Isotopes in Precipitation Calculator, version 3.1 (2023); www.waterisotopes.org.
78. G. J. Bowen, J. Revenaugh, Interpolating the isotopic composition of modern meteoric precipitation. *Water Resour. Res.* **39**, 1299 (2003).
79. P. Greve, L. Gudmundsson, B. Orlowsky, S. I. Seneviratne, Introducing a probabilistic Budyko framework. *Geophys. Res. Lett.* **42**, 2261–2269 (2015).
80. J. T. Abatzoglou, S. Z. Dobrowski, S. A. Parks, K. C. Hegewisch, TerraClimate, a high-resolution global dataset of monthly climate and climatic water balance from 1958–2015. *Sci. Data* **5**, 170191 (2018).
81. V. A. Pedone, C. G. Oviatt, "Chapter 16—Water chemistry changes over time and space in Lake Bonneville during the Post-Stansbury Transgression" in *Developments in Earth Surface Processes*, C. G. Oviatt, J. F. Shroder, Eds. (Elsevier, 2016 20, pp. 442–461.
82. E. T. Crosman, J. D. Horel, MODIS-derived surface temperature of the Great Salt Lake. *Remote Sens. Environ.* **113**, 73–81 (2009).
83. H. L. Bricker, J. B. Bateman, B. Elliott, B. A. Mitsunaga, J. Mering, I. S. Foster, Y. Yanes, E. A. Oches, R. A. Eagle, A. Tripati, A multi-region study of carbonate clumped isotope data from terrestrial snails. *Palaeogeogr. Palaeoclimatol. Palaeoecol.* **628**, 111754 (2023).
84. J. Dong, J. Eiler, Z. An, X. Li, W. Liu, J. Hu, Clumped isotopic compositions of cultured and natural land-snail shells and their implications. *Palaeogeogr. Palaeoclimatol. Palaeoecol.* **577**, 110530 (2021).
85. R. Bao, X. Sheng, C. Li, C. Cui, H. Yan, J. Ji, J. Chen, Calibration of the carbonate clumped isotope thermometer of land snail shells. *Chem. Geol.* **641**, 121773 (2023).
86. S. Kele, S. F. M. Breitenbach, E. Capezzuoli, A. N. Meckler, M. Ziegler, I. M. Millan, T. Kluge, J. Deák, K. Hanselmann, C. M. John, H. Yan, Z. Liu, S. M. Bernasconi, Temperature dependence of oxygen- and clumped isotope fractionation in carbonates: A study of travertines and tufas in the 6–95°C temperature range. *Geochim. Cosmochim. Acta* **168**, 172–192 (2015).
87. H. Kato, S. Amekawa, A. Kano, T. Mori, Y. Kuwahara, J. Quade, Seasonal temperature changes obtained from carbonate clumped isotopes of annually laminated tufas from Japan: Discrepancy between natural and synthetic calcites. *Geochim. Cosmochim. Acta* **244**, 548–564 (2019).
88. N. T. Anderson, J. R. Kelson, S. Kele, M. Daëron, M. Bonifacie, J. Horita, T. J. Mackey, C. M. John, T. Kluge, P. Petschnig, A. B. Jost, K. W. Huntington, S. M. Bernasconi, K. D. Bergmann, A unified clumped isotope thermometer calibration (0.5–1,100°C) using carbonate-based standardization. *Geophys. Res. Lett.* **48**, e2020GL092069 (2021).

Acknowledgments: We thank the Diverse Perspectives on Water Group for their contributions to discussions, and Chairman Donald Ryberg (Siakumne) for discussions. We thank J. Oviatt for samples he helped to collect in Utah and discussions. We thank R. Eagle and the Tripati Lab group (current and past), including J. Lora, V. Petryshyn, and B. Elliott for their contributions. We thank the CDLS for the support. **Funding:** This work was supported by the National Science Foundation EAR-1352212 (to A.T.) and ICER-1936715 (to A.T.), the Heising-Simons Foundation 2021-3137 (to A.T.), 2022-3314 (to A.T.), and 2024-5453 (to A.T.). **Author contributions:** Conceptualization: A.T. Data curation: J.M., A.J.A., and L.C. Formal analysis: J.M., A.J.A., H.-I.L., O.A., and A.F. Funding acquisition: A.T. Investigation: J.M. and A.J.A. Methodology: A.T., D.E.I., J.M., A.J.A., L.C., and A.F. Project administration: A.T. Resources: S.N. Software: D.E.I., J.M., A.J.A., J.S., A.F., and P.V. Supervision: A.T. Visualization: A.J.A., H.L., and A.T. Writing—original draft: J.M., A.J.A., and A.T. Writing—review and editing: J.M., A.J.A., L.C., H.L., J.L., O.A., D.E.I., S.N., A.F., P.V., and A.T. **Competing interests:** The authors declare that they have no competing interests. **Data and materials availability:** All data and code needed to evaluate and reproduce the results in the paper are present in the paper and/or the Supplementary Materials. Stable and clumped isotopic data for each sample can be found in table S1. Reconstructed hydrologic variables for each sample can be found in table S2. Sample and standard replicate level Δ47 data are achieved in Zenodo at https://doi.org/10.5281/zenodo.17674115. This dataset follows the EarthChem Library submission format and will also be archived with the EarthChem repository for domain-specific curation.

Submitted 11 February 2025
Accepted 21 November 2025
Published 1 January 2026
10.1126/sciadv.adw4951

Downloaded from https://www.science.org at Brown University on January 25, 2026